LASER &PHOTONICS REVIEWS

Abstract Inorganic semiconductor-based broadband photodetectors are ubiquitous in imaging technologies such as digital cameras and photometers. Herein we report a broadband organic photodiode (OPD) that has performance metrics comparable or superior to inorganic photodiodes over the same spectral range. The photodiode with an active layer comprised of a poly[*N*-9-heptadecanyl-2,7-carbazole-*alt*-5,5-(4,7-di-2-thienyl-2,1,3-benzothiadiazole)]:[6,6]-phenyl-C_{71}-butyric acid methyl ester bulk heterojunction blend had a dark current < 1 nA/cm^2, specific detectivity of $\sim 10^{13}$ Jones, reverse bias -3 dB frequency response of 100 kHz to 1 MHz, and state-of-the-art Linear Dynamic Range for organic photodiodes of nine orders of magnitude (180 dB). The key to these performance metrics was the use of a thick junction (700 nm), which flattened the spectral response, reduced the dark current and decreased performance variations. The strategy also provides a route to large area defect free monolithic structures for low noise integrated photo-sensing, position determination, or contact, non-focal imaging.

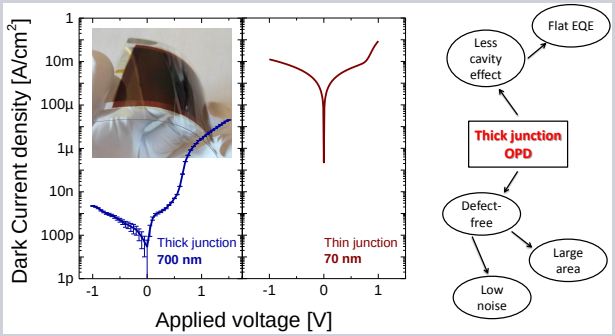

Thick Junction Broadband Organic Photodiodes

Ardalan Armin[1], Mike Hambsch[1], Il Ku Kim[1], Paul L Burn[1], Paul Meredith[1,*], and Ebinazar B Namdas[1]

1. Introduction

The critical parameters that define photodiode performance include responsivity (*R*: A/W), spectral bandwidth (eV or wavelength), dark current (A/cm^2), specific detectivity (D^*: Jones), Linear Dynamic Range (LDR: dB), and frequency response or bandwidth (B: Hz). To date inorganic semiconductors have been the best choice of material for photodiodes, but even these have a trade-off between the performance parameters. For example, while low noise and high frequency inorganic photodiodes are available for applications in imaging, metrology, photometry and position determination [1–4], their spectral bandwidth selectivity is poor (requiring passive band-pass filtering for colour selection [5]) and it is often not technically feasible or economically viable to create inorganic photodiodes for large area applications such as low noise integrated photo-sensing, position determination, or contact, non-focal imaging.

Interest in photodetectors and in particular photodiodes [5] made from organic semiconductors has recently increased due to their potential to deliver simple, low cost processing over large areas [6], high charge carrier photogeneration yields [7], [8] and tunable optical gaps from the UV [8] to NIR [9], [10]. Organic photodiodes comprised of evaporated small molecule [11], conjugated polymer [12], or dendrimer [13] active layers with application in biomedical sensing [14], imaging [15], communications [16], machine vision [17] and control circuits [18] have been widely investigated and reported. Photodiodes are essentially photovoltaic cells that operate under short circuit conditions or reverse bias to improve the charge collection efficiency of photogenerated electrons and holes. However, while there has been some progress in organic photodiode performance including materials giving a broad spectral bandwidth [12], and devices with low dark current [19] [20], high responsivity [8] and detectivity [21], high frequency response [22] and moderate [20] to high [20] [42] Linear Dynamic Range, these parameters are not always found in a single device or indeed active materials combination. To date most organic photodetector designs have been limited to the thin film approach, that is, with an active layer <200 nm in thickness. The problem with devices comprised of thin active layers is that they are low finesse cavities, and their spectral response performance parameters are particularly sensitive to small changes in the layer thicknesses [23, 24]. Furthermore, devices with thin active layers are not amenable to large area devices due to the increased probability of defects.

In this article we demonstrate solution processed and spectrally flat OPDs over the visible band (350 nm to 650 nm) with high detectivity, state-of-the-art Linear Dynamic Range, high frequency response and low noise. The flat spectral response and low dark current is achieved by using a 700 nm thick organic semiconductor layer comprised of poly[*N*-9-heptadecanyl-2,7-carbazole- *alt*-5,5-(4,7-di-2-thienyl-2,1,3-zbenzothiadiazole)]: [6,6] -phenyl-C_{71}-butyric

Centre for Organic Photonics & Electronics, School of Mathematics and Physics and School of Chemistry and Molecular Biosciences, The University of Queensland, St Lucia Campus, Brisbane, QLD 4072 Australia
* Corresponding author: e-mail: meredith@physics.uq.edu.au

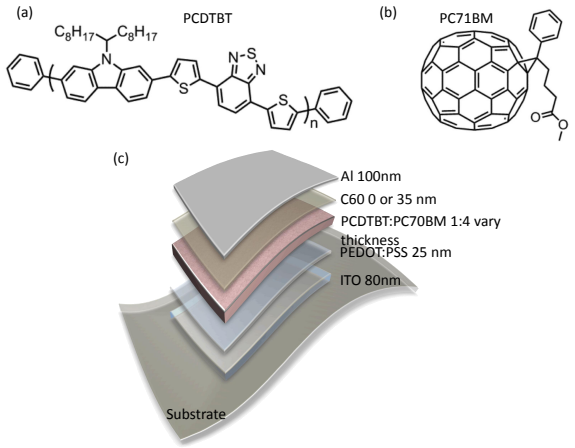

Figure 1 Chemical structures and device architecture used in this work: (a) PCDTBT and (b) PC70BM. (c) The architecture of devices with and without C60 as a blocking layer.

acid methyl ester (PCDTBT:PC70BM). We also report how the charge transporting properties of the active layer affects photodiode performance, in particular the frequency response. Finally, we show how the use of a 700 nm thick active layer enables the fabrication of monolithic large area devices (16 cm^2).

2. Results

The device architectures and the chemical structures of the active materials used in this work are shown in Fig. 1. The photoactive layers were a blend of PCDTBT (electron donor) and PC70BM (electron acceptor) with ratio of 1:4, which have been previously used in efficient [power conversion efficiencies (PCEs) in excess of 6%] thin film ($\sim$90 nm) laboratory scale organic solar cells [7, 24]. Two series of devices were fabricated, differing by whether or not they had a C60 layer between the photoactive layer and the cathode: **Series 1** - ITO (80nm) / PEDOT:PSS (20nm) / PCDTBT:PC70BM (different thicknesses) / Sm (1 nm) / Al (100nm); and **Series 2** - ITO (80nm) / PEDOT:PSS (20nm) / PCDTBT:PC70BM (different thicknesses) / C60 (35 nm) / Sm (1 nm) / Al (100nm). The introduction of the C60 was expected to reduce the dark current by providing a hole blocking/electron transporting layer at the interface with the cathode.

In the first part of the study we varied the thickness of the junction to explore the impact upon external quantum efficiency (EQE). Fig. 2 (a) and (b) shows the results of this study for both **Series 1** and **Series 2** OPDs. For thinner devices (junctions $\sim$100 nm thick), the EQE varies significantly in the visible from 80% at 300 nm to 60% at 450 nm (i.e. the EQE is not spectrally flat and sensitive to thickness variations). By increasing the thickness of the junction to 700 nm, the EQE becomes spectrally flat at 60% over the UV-visible range. When the thin C60 hole-blocking layer (**Series 2**) is added the thinner devices have a different EQE response to the devices without, although the thicker devices show similarly spectrally flat EQEs. The difference in response of the thinner devices arises from the fact that they are low finesse electro-optical cavities where any changes in the layers within the device perturb the optical field distribution, which directly affects the spectral response [24, 25]. Transfer matrix optical modelling (see **Experimental** for details) confirmed the absence of the optical cavity effect in the thick junction devices where presence of the C60 layer does not alter the optical field distribution within the active layer [see Supplementary Information Fig S1). We also compared the photo-response of the OPD devices with several commercial inorganic visible-range photodiodes (Si, GaP and GaAs). In Fig. 2 (c) it can be clearly seen that the 700 nm thick junction OPD device (with a C60 hole blocking layer) at -1 V outperforms the inorganic photodiodes with the response being flatter, with a broader higher EQE and a stronger NIR cut-off than the representative Si photo-diode.

In the next part of the study we investigated the dark current of the devices. Inclusion of the C60 layer was found to suppress the dark current independent of junction thicknesses. The C60 layer blocks the back injection of holes from the cathode at short circuit and at reverse bias operating conditions. This is clearly shown in the current density-voltage (J-V) curves of Fig. 3 where there is typically an order of magnitude difference in dark current density between the **Series 1** and **2** devices (e.g., at -1.0 V reverse bias). Furthermore, Fig. 3 also shows a significant decrease (almost two orders of magnitude) in the dark current density for the 700 nm junction devices versus the 100 nm devices. Table 1 summarises this data at -0.2 V, -0.5 V and -1.0 V as representative reverse bias operational conditions. This suppression of the dark current has a positive impact on the resulting detectivity of the diode, as will be discussed later.

Having established that using a thick photoactive layer can lead to a suppressed dark current and flat EQE over a broad spectral band, we then examined the impact upon other key photodiode performance parameters (D, R, LDR and frequency response). The noise equivalent power (NEP) is the lowest light power detectable by a photodiode and is expressed in terms of i_{noise} , the noise current in unit of $\text{A}/\sqrt{\text{Hz}}$, B the detection bandwidth and R [26]:

$$\text{NEP} = \frac{i_{\text{noise}}\sqrt{B}}{R} = \frac{hci_{\text{noise}}\sqrt{B}}{\text{EQE}\cdot\lambda} : \text{W}, \qquad (1)$$

where, h is Plancks constant, c the speed of light and the wavelength of the incoming light. The NEP can be normalized to the bandwidth to create a device figure of merit:

$$\text{NEP}_\text{B} = \frac{\text{NEP}}{\sqrt{B}} = \frac{i_{\text{noise}}}{R} = \frac{hci_{noise}}{\text{EQE}\cdot\lambda} : \frac{\text{W}}{\sqrt{\text{Hz}}}. \qquad (2)$$

The inverse of the NEP_B is the detectivity of the device, D

$$D = \frac{1}{\text{NEP}_\text{B}} : \frac{\sqrt{\text{Hz}}}{\text{W}}. \qquad (3)$$

Since the photocurrent depends on device area, so do NEP_B and D. To express the noise independent of area, NEP_B

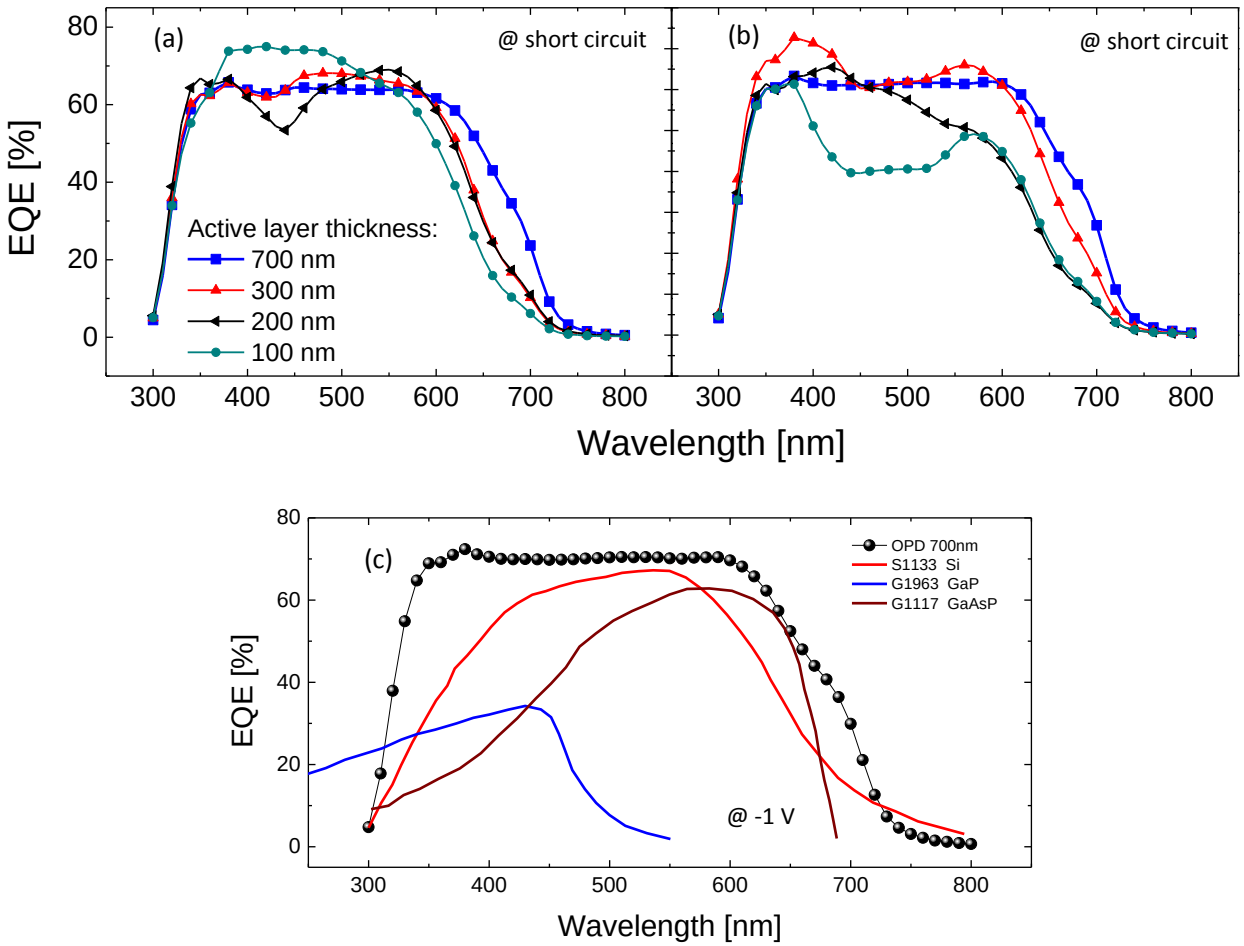

Figure 2 External Quantum Efficiencies (EQEs) of OPDs and a comparison of spectral response of a 700 nm thick junction OPD with commercially available inorganic visible photodiodes: (a) and (b) EQE spectra of series 1 and 2 devices respectively with varying junction thicknesses. Due to optical interference effects, the spectral shape of the EQE varies with the thickness. In thick devices (junctions ∼700 nm) with and without C60, spectrally flat EQE (∼60%) is obtained over the visible band. (c) EQE of a PCDTBT:PCBM OPD with junction thickness of 700 nm (with C60 hole blocking layer) biased at -1.0 V compared with commercial inorganic visible photodiodes (data from Hamamatsu datasheets). The OPD exhibits a high external quantum efficiency of 70%, which is constant over the visible spectrum while the inorganic photodiodes cover a narrower bandwidth with lower and non-flat EQE.

can be further normalized to the device area A to yield the specific detectivity $D^{\star}$ as

$$D^{\star} = \frac{\sqrt{A}}{\mathrm{NEP_B}} : \frac{\mathrm{cm}\sqrt{\mathrm{Hz}}}{\mathrm{W}}. \tag{4}$$

Considering Eq. (2) and (4), $D^{\star}$ can finally be rewritten as:

$$D^{\star} = \frac{\lambda\sqrt{A}\cdot\mathrm{EQE}}{hc\cdot i_{\mathrm{noise}}} : \frac{\mathrm{cm}\sqrt{\mathrm{Hz}}}{\mathrm{W}}. \tag{5}$$

The unit $\frac{\mathrm{cm}\sqrt{\mathrm{Hz}}}{\mathrm{W}}$ is also called the *Jones*. To accurately evaluate the specific detectivity using Eq. (5) it is necessary to determine i_{noise} at the detection frequency. The noise current is commonly expressed as a summation of the shot noise (the fluctuations of the current due to the discrete nature of the Poissonian distributed electrons) and thermal noise (Johnson-Nyquist fluctuations) [27] as follows:

$$\langle i^2_{\mathrm{noise}}\rangle = 2ei_dB + 4kT\frac{B}{R_{\mathrm{sh}}}, \tag{6}$$

where e is the elementary charge, k the Boltzmann constant, T absolute temperature and R_{sh} the shunt resistance of the photodiode. However, it should be noted that the noise determined from Eq. (6) may underestimate the noise level [21] and result in ambiguous specific detectivity [12] due to other noise sources such as flicker. Fig. 4(a) shows the measured noise current along with the shot noise and the thermal noise components as a function of dark current for an optimised 700 nm junction device with a C60 hole blocking layer. The noise current was measured by integrating the Fast Fourier Transform (FFT) of the dark current up to measurement

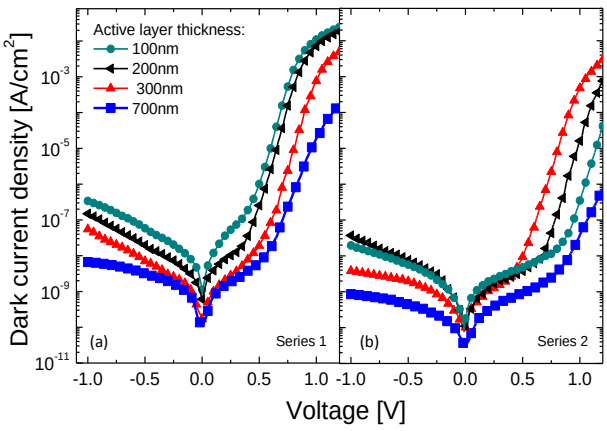

Figure 3 Current density-voltage (J-V) characteristics of OPDs with different junction thicknesses with and without C60 hole blocking layer: (a) J-V curves in the dark for series 1 OPDs. By increasing the junction thickness, the dark current can be significantly decreased. (b) J-V curves in the dark for series 2 devices (with C60 hole blocking layer). In a thick device, the dark currents reduced by an order of magnitude to <1 nA/cm^2.

Table 1 The dark current density for photodiodes with different active layer thickness without/with C60 hole blocking layer [nA].

thickness [nm]	at -0.2 V	at -0.5 V	at -1.0 V
100	160/60	50/6	315/17
200	5.8/1.8	17.0/6.5	100/30
300	2.0/0.7	7.0/1.8	55/4
700	1.35/0.16	3.00/0.42	6.6/0.8

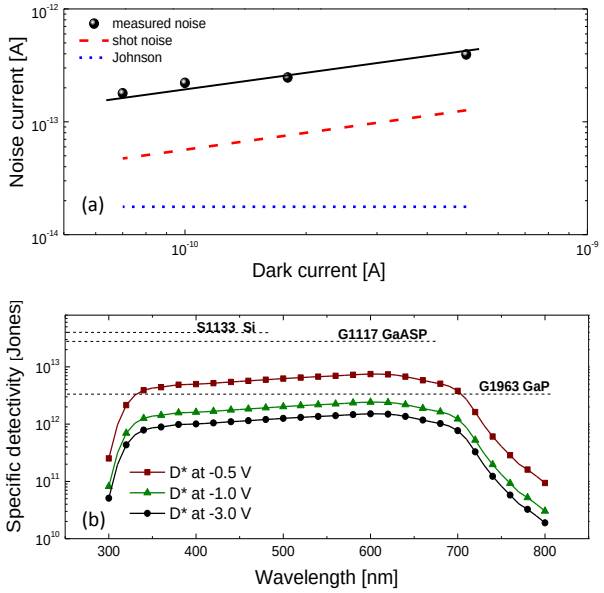

Figure 4 Noise currents and detectivity of 700 nm thick PCDTBT:PC70BM OPDs: (a) The measured noise current (black rectangles), shot noise (red dashed line) and thermal Johnson-Nyquist noise (blue dotted line) for a 700 nm thick junction device with a C60 hole blocking layer over a 100 Hz bandwidth. The actual measured noise is only a few times higher than the shot noise and an order of magnitude higher than the thermal noise. (b) The measured specific detectivity (Jones) as a function of wavelength and bias voltage. Detectivities of commercial inorganic visible photodiodes are presented for direct comparison (the detectivities of inorganic photodiodes are inferred from the dark current at -1.0 V: Data from Hamamatsu datasheets). The detectivity of the OPD approaches 10^{13} Jones at a bias voltage of -0.5 V.

frequency of 120 Hz at which the noise floor was reached (for details see Supplementary Information Fig. S2). The shot noise and the thermal noise were calculated from Eq. (6). The shunt resistance was evaluated from the J-V curve and was $\sim$3 GΩ (for details see the Supplementary Information Fig. S3). The noise current in the thick junction OPDs was only a few times higher than the shot noise, and there was only a minimal contribution from thermal noise. Using the measured noise current as a function of the dark current (or applied voltage), the specific detectivity was calculated and is shown in Fig. 4 (b). The specific detectivity is bias voltage dependent as expected due to the increase in the dark current under reverse bias voltage conditions. For our 700 nm thick junction device with a C60 hole blocking layer $D^\star$ approaches 10^{13} Jones. This is very close to the performance of typical inorganic photodetectors [see Supplementary Information Table S1 and Fig. 4 (b).

We next investigated the Linear Dynamic Range (LDR), which is the range in dB of input light power (irradiance) over which the responsivity is constant. The photocurrent *versus* input light power (irradiance) at 532 nm for a typical optimised 700 nm thick junction device with C60 hole blocking layer is shown in Fig. 5. The baseline at the lower end of the range was limited by the sensitivity of our measurement equipment to 20 pA/cm^2. The photocurrent was found to increase linearly with irradiance up to 10^{-1} W/cm^2, i.e., over nine orders of magnitude. Note the actual lower limit of the LDR is potentially (not necessarily [42]) defined by the noise current, which in our OPD would deliver an LDR of eleven orders of magnitude equal to the LDR of currently available inorganic photodiodes (also shown in Fig. 5). It is generally accepted in organic semiconductor photo-diodes and solar cells that the upper limit of linearity (between the input irradiance and photocurrent) is defined by bimolecular recombination of the photogenerated charge carriers [28]. The so-called deviation current $j_{\rm dev}$ (at which bimolecular recombination is dominant at high enough charge carrier concentration [29]) defines the limit of linearity and hence the upper end of the LDR. Based upon the $j_{\rm dev}$ extracted from Fig. 5 and the measurable lower limit of photocurrent, the LDR was calculated to be

$$\mathrm{LDR} = 20\log\frac{j_{\rm dev}}{j_{\rm min}} = 180\mathrm{dB}, \qquad (7)$$

which is amongst the highest value reported to date for an OPD (see Supplementary Information Table 1.)

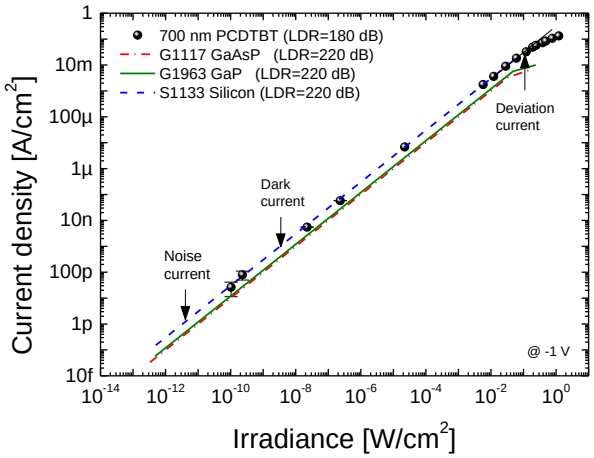

Figure 5 Linear Dynamic Range (LDR) of a 700 nm PCDTBT:PC70BM OPD and commercially available visible photodiodes: Photocurrent measured at -1.0 V reverse bias voltage as a function of incident light irradiance (excitation wavelength = 532 nm) for the 700 nm thick OPD (with C60 hole blocking layer). Also shown are LDRs of commercially available visible photodiodes (data from Hamamatsu datasheets). Deviation from linearity is observed at 0.03 A/cm^2 which is the upper limit of the linear dynamic range. The lower limit of the linear dynamic range is theoretically the noise current. These upper and lower limits indicate an LDR ~11 orders of magnitude or 220 dB, which is equal to those of GaP, GaAsP and Si photodiodes. The minimum photocurrent of this OPD measured in our laboratory (with equipment limitations) was measured at 30 pA/cm^2, which yields a linear dynamic range of 180 dB, very close to values in inorganic photodiodes.

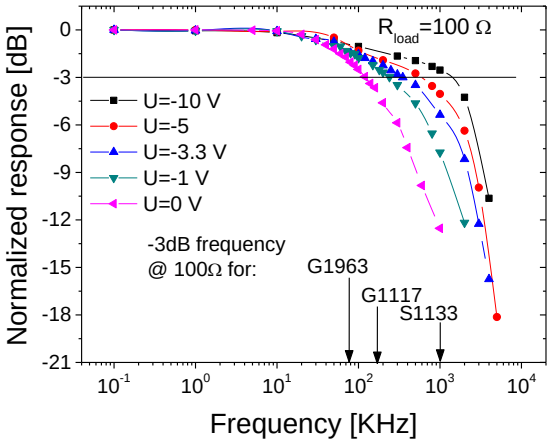

Figure 6 Frequency response of 700 nm thick PCDTBT:PC70BM OPD: Normalized photoresponse under modulated light illumination (irradiance, L=2.2 mW/cm^2 and wavelength, λ=520 nm) as a function of modulation frequency (Bode plot) for a 700 nm thick junction OPD with C60 blocking layer. The -3 dB bandwidth is 120 KHz at the short circuit condition and can be increased to 1 MHz in reverse bias (-5.0 V). Also shown are the -3 dB response of three commercial visible inorganic photodiodes (with similar device area of 0.2 cm^2) for comparison.

We also measured the frequency response or bandwidth (B) as the last figure of merit of our optimised thick junction OPDs as a function of reverse bias voltages. The bandwidth is defined as the frequency of input light modulation at which the photo-response is -3dB lower than the continuous wave (CW) response. The -3dB bandwidth is limited by the carrier transit time, characteristic RC-time or both [30], and is given by

$$\frac{1}{f_{-3\mathrm{dB}}^2} = \frac{1}{f_t^2} + \frac{1}{f_{\mathrm{RC}}^2}, \tag{8}$$

where f_t and f_{RC} are the carrier transit time limited and RC limited bandwidths respectively and are defined as [31]

$$f_t = \frac{3.5}{2\pi t_{\mathrm{tr}}} \tag{9}$$

and

$$f_{\mathrm{RC}} = \frac{1}{2\pi \mathrm{RC}}, \tag{10}$$

where t_{tr} is the carrier transit time, R the total series resistance including the photodiode series resistance, sheet resistance, contact resistances and load resistances in the measurement circuit. The photo-response of the 700 nm junction (with C60 hole blocking layer) was measured as a function of modulation frequency of input light at an irradiance of 2.2 mW/cm^2, wavelength =520 nm and load resistance of 100 Ω and is shown in Fig. 6. At the short circuit condition the -3dB frequency was found to be 120 KHz, which increases to 1 MHz under reverse bias (-5.0 V). In the same figure, the -3dB frequency responses of three commercial visible inorganic photodiodes are also included for comparison. At -1 V our 700 nm OPD delivers -3 dB frequency higher or comparable to inorganic photodetectors operating in visible spectral range.

Finally, we made a preliminary investigation of whether the thick junction concept could be extended to large area OPDs on flexible substrates. To this end we fabricated a 16 cm^2 monolithic device (*i.e.*, a single active region) on a typical plastic electrode structure (PET-ITO: see Supplementary Information). We observed a very low dark current, in fact equivalent to that observed in the small lab-scale OPDs of < 1 nA/cm^2 with a flat, broad band spectral response. In contrast, a thin junction OPD of comparable size had a dark current six orders of magnitude larger (Fig. S4).

3. Discussion

Our results clearly show that employing thick bulk heterojunctions to OPDs can deliver devices with very low dark currents and spectrally flat responses over the visible. The flattening of the EQE spectral response occurs because the absorption path length in the thick junction (αd) exceeds the limit where, for all wavelengths within the band edge, the Beer-Lambert Law applies, *i.e.*, $I(x) = I_0 \mathrm{e}^{-\alpha x}$ and the optical field, $I(x)$ falls off exponentially as a function of the propagation distance, where α is the absorption coefficient, x position coordinate in the active layer and I_0 the incident

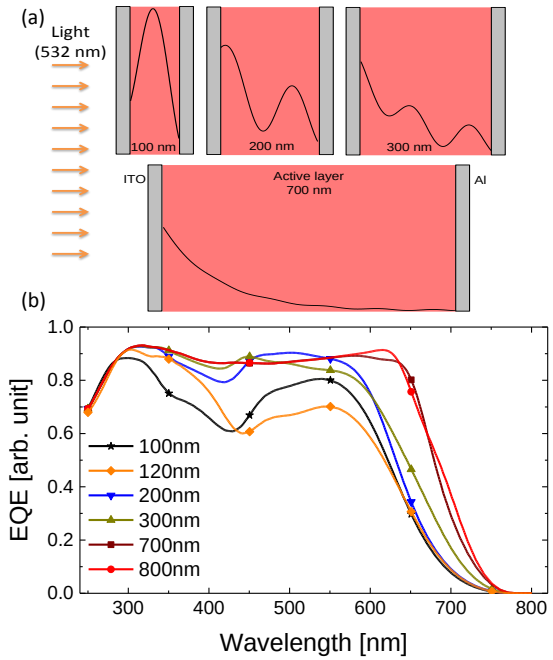

Figure 7 Comparison of absorbed photon distribution profiles and simulated EQE in PCDTBT:PC70BM devices with different junction thicknesses: (a) Simulated absorbed photon distribution within the OPD active layers as a function of junction thickness under light illumination (excitation at 532 nm wavelength). As the thickness increases, the distribution of absorbed photons switches from the interference-governed regime to Beer-Lambert like behaviour. (b) Simulated EQE spectra for PCDTBT:PC70BM OPDs for a blend ratio of 1:4 assuming 100% internal quantum efficiency as a function thickness. In the thin junctions the EQE is sensitive to thickness variations while in devices thicker than 600 nm the EQE becomes spectrally flat and insensitive to thickness variations.

optical field amplitude. Under such circumstances there is no interference between the forward propagating waves and backward propagating waves produced by reflections from the electrodes in the cavity. When the absorption path length is thin, *i.e.*, below the limit where the Beer-Lambert Law applies, interference effects impact the shape of the optical field distribution in the junction and hence the EQE of the device. This is clearly demonstrated in Fig. 7 (a) which shows absorbed photon distributions as a function of the normalized position (into the active layer) under 532 nm illumination for various junction thicknesses. These profiles were obtained using the transfer matrix approach [25, 32]. In Fig. 7 (b) we have translated the photon absorption to the corresponding EQEs calculated assuming a wavelength independent Internal Quantum Efficiency [24, 33, 34]. Flattening of the EQE occurs for thicker junctions >600 nm in line with our experimental results (with or without the C60 layer). Importantly, the EQE spectra of the thick junctions are insensitive to the thickness variations that naturally occurs during fabrication of solution processed OPDs.

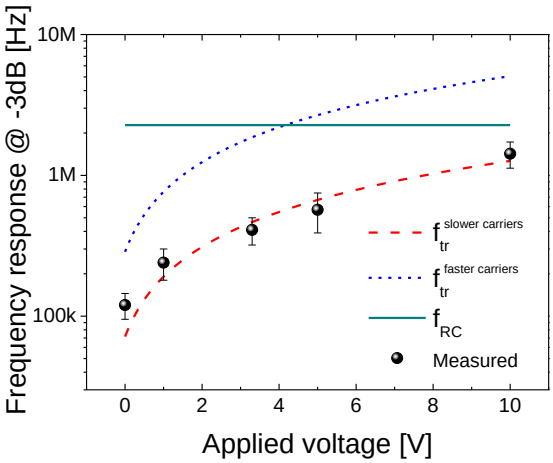

Figure 8 Correlating -3 dB bandwidth with slower carriers transit time: The measured -3 dB bandwidths as a function of reverse bias voltage along with calculated slower and faster carrier transit time limited bandwidths (f_t) and RC limited bandwidths (f_{RC}). These results show that the actual bandwidth of the detector is not limited by RC nor the faster carrier transit time. The bandwidth calculated based on the slower carrier transit time agrees with the experimentally measured bandwidth.

Optimised 700 nm OPDs with the C60 hole blocking layer were shown to possess impressive performance metrics relevant to applications such as photographic imaging: dark current <1 nA/cm^2, detectivity of 1×10^{13} Jones, reverse bias -3dB frequency response of 100 kHz to 1MHz, and state-of-the-art LDR of 180 dB, which compare favorably with current commercial inorganic photodiodes. Use of a thin C60 hole-blocking layer in combination with this thick junction gave rise to the very low dark current densities both in small (0.2 cm^2) and large area (16 cm^2) monolithic OPDs on a plastic substrate. One of the main reasons for such low dark currents in thick junctions is that, they are less affected by defects, pinholes, bubbles and ITO spikes. The probability of having a defect free device can be written $P = \mathrm{e}^{-A.\mathrm{DD}}$ assuming that the defects are distributed in a Poissonian [35] manner, where A is the area of the cell and DD the density of defects. This is an absolutely critical consideration for scaling not only of OPDs, but large area organic solar cells also.

The upper limit of the LDR was found to occur at quite high photocurrents. To understand the origin of the excellent LDR we carried out high intensity photo-CELIV measurements (see Fig. S5), which showed that bimolecular recombination was 15 times suppressed when compared to the Langevin rate. Finally, to elucidate the reason for the good frequency response of the OPD we undertook further charge transport studies. The charge carrier transport in a photodiode is related to the faster and slower carrier mobilities in the semiconductor junction. Faster and slower carrier mobilities of an optimised 700 nm OPD were measured by photo-CELIV [36] and the Double Injection (DI) [37] technique (see Supplementary Information Fig. S6 and S7

for details). An electron mobility of $\mu_e = 3 \times 10^{-3} \mathrm{cm}^2/\mathrm{Vs}$ and hole mobility of $\mu_h = 3 \times 10^{-4} \mathrm{cm}^2/\mathrm{Vs}$ were obtained. The electron mobility compares well with previously measured values for PCDTBT:PC70BM based solar cells with an operational thickness of 100 nm [38, 39]. Our measured value for the hole mobility in the thick junction OPDs is an order of magnitude higher than those previously reported for standard thin junctions [38], which is plausibly due to differences in molecular weight and the resulting morphology of thin versus thick junctions. Although PCDTBT films have been known to have an amorphous structure, it has recently been shown that high molecular weight co-polymers (see **Experimental** for molecular weight) exhibit short-range intermolecular aggregation allowing efficient long-range charge transport [40]. The frequency response of our thick junction devices was found not to be limited by the characteristic RC-time. The capacitance of the photodiode was found to be 3.7 nF/cm^2. f_{RC} and f_t for faster and slower carriers were calculated from Eq.(9) and (10) using the mobility values (note that the transit time is $t_{\mathrm{tr}} = d/\mu E$, where d is the average distance travelled by the carriers before collection the electrodes, the mobility and E the electric field in the device). In Fig. 8 the calculated f_t (for faster and slower carriers) and f_{RC} are shown along with the measured $f_{-3\mathrm{dB}}$ from Fig. 6 as a function of the reverse bias voltage. This data confirms that the photodiode speed is not limited by the RC-time in this case but rather the slower carrier mobility. In fact, the measured frequency response was found to be in strong agreement with that calculated from the slower carrier mobility (transit time) indicating this to be the source of the device speed upper limit (100 KHz at short circuit up to 1 MHz at -5.0 V reverse bias, and more than adequate for imaging and photometric applications). This approach can be employed to predict the bandwidth of OPDs provided charge transport is well studied in the system.

4. Conclusion

In conclusion, a clear understanding of organic solar cells and photodiodes as low finesse, thin film cavity devices has delivered a new structure-performance control tool for OPDs namely the thick junction concept. The strategy can be scaled to deliver lower defect density, low dark current large area devices in a monolithic geometry. In principle, this is highly beneficial for manufacturing prospects since the approach simplifies processing and architectures, thus reducing complexity and cost with higher yields.

5. Experimental

Materials: PCDTBT ($\bar{\mathrm{M}}$w=122200 g/mol, PDI=5.4) was purchased from SJPC, Canada. The molecular weight of PCDTBT was determined with Gel Permeation Chromatography (GPC) in 1,2,4-trichlorobenzene at 135 C. PC70BM and C60 were purchased from American Dye Source, Inc., Canada and used without further purification.

Sample preparation:The glass substrates with pre-etched ITO for bulk heterojunction OPDs were purchased from Kintec and mechanically cleaned by scrubbing using a soft cloth in a 90 C warm Alconox (detergent) solution. Cleaning was followed by sequential ultrasonication in Alconox, de-ionized water, acetone, and 2-propanol. For the flexible, large area OPD poly(ethylene terephthalate) (PET) substrates with an indium tin oxide (ITO) layer from Visiontek (ITOPET50) were used. The ITO electrode was patterned by etching with a 5 M hydrochloric acid solution. After etching the substrate was cleaned sequentially in detergent, de-ionized water and 2-propanol. After drying all the substrates under a nitrogen flow, a poly(3,4-ethylenedioxythiophene) :poly(styrene sulfonate) (PEDOT:PSS) (Baytron P VPAl4083) film was spin-coated at 5000 rpm. The resulting 30 nm thin layer was baked at 170 C for 10 minutes in air. All the device edges were cleaned with a wet cloth to prevent lateral current leakage through the PEDOT:PSS. Solutions of PCDTBT and PC70BM were prepared in 1,2-dichlorobenzene and combined at 90 C to obtain a PCDTBT:PC70BM ratio in solution of 1:4 w/w and a total material concentration of 35 mg/ml. The PC70BM solution was filtered before mixing with PCDTBT. The solution was immediately removed from the hot-plate and placed on a metal surface at room temperature to achieve fast cooling. This fast cooling protocol increased the viscosity of the solution and as explained in citation [41] enabled us to obtain very thick devices (>500 nm) by spin coating. 700 nm Thick film samples were prepared with spin speed of 600 rpm. The thinner devices were made at higher spin speeds (see Supplementary Information for details Fig S8). BHJ layer thicknesses were measured with a Veeco Dektak 150 profilometer. For series 2 devices a 35nm layer of C60 was deposited by thermal evaporation under a vacuum of 10^{-6} mbar. Finally, 1 nm of samarium followed by 100 nm of aluminum was thermally deposited under the same vacuum conditions to complete the devices. The resulting device areas were 0.2 cm^2 with 6 devices per substrate and 16 cm^2 with 1 device per substrate for the large area monolithic OPDs.

External Quantum Efficiency (EQE) and transfer matrix simulations:External Quantum Efficiencies were measured using a PV Measurements Inc. QEX7 setup at 120 Hz. The optical field distributions with the photodiodes were simulated using a computer code based on the transfer matrix method developed by van de Lagemaat et al. from the National Renewable Energy Laboratory (NREL). For these simulations optical constants (refractive index and extinction coefficients) of the all the materials in the structure are required. In this regard, we performed spectroscopic ellipsometry (SE) measurements for PCDTBT:PC70BM films on silicon wafers. Optical constants of the other layers have been measured previously and / or have been reported in the literature. The SE measurements were performed with a vacuum ultraviolet-variable angle spectroscopic ellipsometer (VUV-VASE) (GEN II) J.A. Woollam with autoretarder. J.A.Woollam WVASE32 software was used to fit the data. Optical constants for PCDTBT:PC71BM are shown in Fig S9.

Dark/photo current and LDR measurement: Dark currents and photocurrents were measured by using an Agilent semiconductor analyser B1500A. The devices were mounted on an optical table in a Faraday cage with a small aperture for the laser beam. Triax leads were used to minimize the measurement noise. An ITO on glass panel that was electrically connected to the cage by silver paste to further reduce the electrical noise covered the aperture. A Second Harmonic Nd:YAG laser operating continuously at 532 nm was used as the illumination source with a series of neutral density filters purchased from Thorlabs and Holmarc for the LDR measurements. The signal was acquired at 120 Hz.

Frequency response (bandwidth) and transient measurements:Frequency measurements were made using a NSPG500DS Nichia green LED modulated by using an arbitrary wave generator Agilent 33250A function generator. The photocurrent response of the photodiode was recorded using a digital storage oscilloscope (LeCroy Waverunner A6200). Double injection transients were recorded by the same oscilloscope. For the double injection experiment the photodetector was biased in the forward direction by an Agilent 33250A function generator and the current was read out from across a 10 load resistance. Photo-CELIV was performed using a pulsed third-harmonic Nd:YAG laser (Quantel Brio) working at a wavelength of 355 nm and pulse duration of 5 ns. The laser beam was attenuated by a neutral density lter set purchased from Thorlabs. A delay generator (Stanford Research System DG535) and an arbitrary waveform generator (Agilent 33250A) were used to generate CELIV triangle pulse in reverse bias with adjustable voltage slope and time delay.

Acknowledgements. AA is funded by University of Queensland International scholarship. PLB and PM are supported by University of Queensland Vice Chancellors Senior Research Fellowships. EBN is an Australian Research Council Future Fellow. We acknowledge support from The University of Queensland (Strategic Initiative Centre for Organic Photonics & Electronics). This work was performed in part at the Australian National Fabrication Facility Queensland Node (ANFF-Q) - a company established under the National Collaborative Research Infrastructure Strategy to provide nano- and microfabrication facilities for Australias researchers. AA prepared the samples and performed the experiments and analysis. AA and MH prepared the large area samples and performed the large area OPD measurements. AA and PM developed the thick junction, low finesse cavity concept. AA, PLB, EBN and PM designed the experiments and research plan. All authors contributed to the preparation of the manuscript and have given approval to the final version of the manuscript.

Key words: broadband photodiodes, large area photodiodes, micro-cavities, organic photodiodes, thick bulk heterojunctions

References

[1] N. Daldosso, and L. Pavesi. Laser & Photon. Rev. **3**, 508–534 (2009).
[2] Y. Yang, Y. Wu, R. Farrell, P. A. Dokhale, K. S. Shah, S. R. Cherry, Physics in medicine and biology **56**, 6327 (2011).
[3] M. A. Taylor, J. Janousek, V. Daria, J. Knittel, B. Hage, H.-A. Bachor, W. P. Bowen, Nat. Photon. **7**, 229–233 (2013).
[4] C. W. Stubbs, P. Doherty, C. Cramer, G. Narayan, Y. J. Brown, K. R. Lykke, J. T. Woodward, J. L. Tonry, The Astrophysical Journal Supplement Series **191**, 376 (2010).
[5] K. J. Baeg, M. Binda, D. Natali, M. Caironi, Y. Y. Noh, Adv. Mater. **25**, 4267–4295 (2013).
[6] H. Jin, C. Tao, M. Velusamy, M. Aljada, Y. Zhang, M. Hambsch, P. L. Burn, P. Meredith, Adv. Mater. **24**, 2572–2577 (2012).
[7] S. H. Park, A. Roy, S. Beaupr, S. Cho, N. Coates, J. S. Moon, D. Moses, M. Leclerc, K. Lee, A. J. Heeger, Nat. Photon. **3**, 297–302 (2009).
[8] Y. Fang, F. Guo, Z. Xiao, J. Huang, Adv. Opt. Mater. **2**, 348–353 (2014).
[9] F. Liu, Y. Gu, C. Wang, W. Zhao, D. Chen, A. L. Briseno, T. P. Russell, Adv. Mater. **24**, 3947–3951 (2012).
[10] J. Peet, J. Kim, N. E. Coates, W. L. Ma, D. Moses, A. J. Heeger, G. C. Bazan, Nat. Mat. **6**, 497–500 (2007).
[11] S.-h. Wu, W.-l. Li, B. Chu, Z.-s. Su, F. Zhang, C. Lee, Appl. Phys. Lett. **99**, 023305 (2011).
[12] X. Gong, M. Tong, Y. Xia, W. Cai, J. S. Moon, Y. Cao, G. Yu, C.-L. Shieh, B. Nilsson, A. J. Heeger, Science **325**, 1665–1667 (2009).
[13] R. D. Jansen-van Vuuren, A. Pivrikas, A. K. Pandey, P. L. Burn, J. Mater. Chem. C **1**, 3532–3543 (2013).
[14] N. M. M. Pires, T. Dong, Biomedical Circuits and Systems Conference (BioCAS) IEEE 105-108 (2013).
[15] D. Baierl, L. Pancheri, M. Schmidt, D. Stoppa, G.-F. Dalla Betta, G. Scarpa, P. Lugli, Nat. Comm. **3**, 1175 (2012).
[16] J. Clark, G. Lanzani, Nat. Photon. **4**, 438–446 (2010).
[17] R. J. van Vuuren, K. Johnstone, S. Ratnasingam, H. Barcena, P. Deakin, A. Pandey, P. Burn, S. Collins, I. Samuel, Appl. Phys. Lett. **96**, 253303 (2010).
[18] D. Li X. Liu, G. Dong, L. Duan, D. Zhang, H. Zhao, l. Wang and Y. Qiu, Laser & Photon. Rev. **8**, 316-323 (2014).
[19] T. N. Ng, W. S. Wong, M. L. Chabinyc, S. Sambandan, R. A. Street, Appl. Phys. Lett. **92**, 213303 (2008).
[20] X. Liu, H. Wang, T. Yang, W. Zhang, Z. Gong, ACS Appl. Mater. Inter. **4**, 3701–370 (2012).
[21] F. Guo, B. Yang, Y. Yuan, Z. Xiao, Q. Dong, Y. Bi, J. Huang, Nat. Nano. **7**, 798–802 (2012).
[22] P. Peumans, V. Bulovi, S. Forrest, Appl. Phys. Lett. **76**, 3855–3857 (2000).
[23] F. Nickel, C. Sprau, M. F. Klein, P. Kapetana, N. Christ, X. Liu, S. Klinkhammer, U. Lemmer, A. Colsmann, Solar Energy Materials and Solar Cells. **104**, 18–22 (2012).
[24] A. Armin, M. Velusamy, P. Wolfer, Y. Zhang, P. L. Burn, P. Meredith, A. Pivrikas, ACS Photonics, **1**, 173181 (2014).
[25] J. Mescher, N. Christ, S. Kettlitz, A. Colsmann, U. Lemmer, Appl. Phys. Lett. **101**, 073301–073301-4 (2012).
[26] S. M. Sze, Semiconductor DevicesPhysics and Technology (Wiley, Toronto, 1985).
[27] P. Bhattacharya, Semiconductor optoelectronic devices. (Prentice-Hall, Inc., 1994).
[28] K. Maturov, S. S. Van Bavel, M. M. Wienk, R. A. Janssen, M. Kemerink, Adv. Func. Mater. **21** 261–269 (2011).
[29] R. Street, M. Schoendorf, A. Roy, J. Lee, Phys. Rev. B **81** 205307 (2010).
[30] K. Kato, S. Hata, J. Yoshida, A. Kozen, Indium Phosphide and Related Materials 254–257, IEEE Fourth International Conference (1992).

[31] K. Kato, Microwave Theory and Techniques, IEEE Transactions **47**, 1265–1281 (1999).
[32] P. Peumans, A. Yakimov, S. R. Forrest, J. Appl. Phys. **93**, 3693 (2003).
[33] K. Vandewal, S. Albrecht, E. T. Hoke, K. R. Graham, J. Widmer, J. D. Douglas, M. Schubert, W. R. Mateker, J. T. Bloking, G. F. Burkhard, A. Sellinger, J. M. J. Fréchet, A. Amassian, M. K. Riede, M. D. McGehee, D. Neher, A. Salleo, Nat. Mater. **13**, 6368 (2014).
[34] A., Steve, K. Vandewal, J. R. Tumbleston, F. S. U. Fischer, J. D. Douglas, J. M. J. Fréchet, S. Ludwigs, H. Ade, A. Salleo, D. Neher. Advanced Materials DOI: 10.1002/adma.201305283, (2014).
[35] J. Agostinelli, M. Kowarz, L.-S. Liao, Google Patents (2004).
[36] A. Mozer, N. Sariciftci, L. Lutsen, D. Vanderzande, R. sterbacka, M. Westerling, G. Juka, Appl. Phys Lett., **86**, 112104–112104-3 (2005).
[37] A. Armin, G. Juska, B. W. Philippa, P. L. Burn, P. Meredith, R. D. White, A. Pivrikas, Adv. Ener. Mater. **3**, 321-327 (2012).
[38] A. Armin, G. Juska, M. Ullah, M. Velusamy, P. L. Burn, P. Meredith, A. Pivrikas, Adv. Ener. Mater. **4**, 1300954 (2014).
[39] T. M. Clarke, J. Peet, A. Nattestad, N. Drolet, G. Dennler, C. Lungenschmied, M. Leclerc, A. J. Mozer, Org. Elec. **13**, 2639–2646 (2012).
[40] R. Noriega, J. Rivnay, K. Vandewal, F. P. V. Koch, N. Stingelin, P. Smith, M. F. Toney, A. Salleo, Nat. Mater. **12**,10381044 (2013).
[41] P. Wolfer, A. Armin, A. Pivrikas, M. Velusamy, P. L. Burn, P. Meredith, J. Mater. Chem. C **2**, 71–77 (2014).
[42] F. Guo, Z. Xiao, J. Huang, Adv. Opt. Mater. C **1**, 289–294 (2013).